Mechanism of charge accumulation in Poly(heptazine imide)

Goichiro Seo,*[a] Ryoma Hayakawa,[b] Yutaka Wakayama,[b] Ryosuke Ohnuki,[a] Shinya Yoshioka,[a] and Kaname Kanai[a]

a. Department of Physics and Astronomy, Faculty of Science and Technology, Tokyo University of Science, 2641 Yamazaki, Noda, Chiba 278-8510, Japan

b. Research Center for Materials Nano architectonics (MANA), National Institute for Materials Science (NIMS), 1-1 Namiki, Tsukuba, Ibaraki 305-0044, Japan.

* Corresponding author: 6222701@ed.tus.ac.jp

1. Note 1.

1-1 Methods for synthesizing samples.

melem:

Melem was obtained as a single crystal of melem hydrate after calcination of melamine(5g, purity: 99.0% Wako Pure Chem., Ind., Ltd., 139-00945) in a tube furnace(KTF035N1 / Koyo Thermo Systems Co.). Calcination in a tube furnace was performed with a program of temperature increase to 310°C at 1°C/min, followed by holding for 5 hours and then natural cooling. The resulting product was washed with DMF and acetone and dried at 150°C for 24 hours. The dried sample was dissolved in DMSO to obtain melem hydrate single crystals by vapor diffusion method.

melon:

Melon was synthesized in the same way as Melem, in a tube furnace; Melamine (3 g) was placed at the bottom of a quartz test tube and calcined with a program of increasing temperature to 550°C at 1°C/min, holding for 5 hours, and decreasing temperature at 2°C/min.

K-PHI:

K-PHI was obtained by mixing the previously described Melon (0.3 g) and KSCN (0.15 g, purity: 98.0% Wako Pure Chem., Ind., Ltd., 164-04555) and calcining them. The boat was calcined in a tube furnace with a program of temperature increase at 30°C/min, hold for 1 hour, temperature increase at 30°C/min, hold for 30 minutes, and temperature decrease at 2°C/min.

1-2 Method of fabricating films

Melem thin film:
Melem hydrate single crystals synthesized by the method described above were placed in an aluminum crucible and evaporated onto a substrate in an ultra-high vacuum (10^{-6} Pa) to fabricate a 30 nm thin film. The substrate was Au(300 nm)/Si(100).

K-PHI nanosheet:
K-PHI synthesized by the method described above was dispersed in NMP and sonicated for 60 hours for chemical cleavage. The resulting dispersion was separated in a centrifuge overnight, and the supernatant liquid was taken as K-PHI nanosheet dispersion (Fig. S1(b)).

K-PHI nanosheet film:
Chlorobenzene was mixed with the K-PHI nanosheet dispersion at a ratio of 60 vol%, and the nanosheet was precipitated by centrifugation overnight. The resulting concentrated liquid of nanosheet was dropped onto the substrate to fabricate the K-PHI film. Then, UV-O_3 cleaning performed on the K-PHI film (UV253E; Filgen). The cleaning time was 30 minutes, and the cleaning chamber was replaced with oxygen before the cleaning.

PTCDI:
In the same way as Melem, PTCDI (3, 4, 9, 10-Perylenetetracarboxylic Diimide >95% Tokyo Chemical Industry Co., Ltd. P0984) was fabricated by 30 nm deposition in an ultra-high vacuum. The substrate is also the same.

1-3 Measurement methods

XRD:
XRD was performed using Smart lab. (Rigaku), and Cu Ka = 0.15496 nm) was used as the X-ray source.

TEM:
TEM was measured using a JEM-2100F (JEOL) with an acceleration voltage of 80 kV and spherical aberration correction Cs = 0.5 mm. Cu300 mesh (EM Japan Co., Ltd. U1015-F10) was used for the grid.

XPS, UPS and IPES:
XPS was performed using JPS-9030 (JEOL) monochromatized Al Ka ($h\nu$=1486.6 eV) was used as the X-ray source. UPS was a self-made device in the laboratory. The analyzer was a SES200 (SCIENTA), and the light source was He Ia ($h\nu$=21.22 eV). IPES was performed on the same sample in the same apparatus as the UPS, and measurements were made on a PSP Vacuum Technology equipment was used for the measurements. The band-pass detector consisted of a NaCl-coated Channeltron behind a SrF2 window and detected photons at $h\nu$ = 9.3 eV.

UV-vis measurement:
UV−vis was performed using V-670 (JASCO Corporation) with an integrating sphere and the spectra obtained by transmission method.

AFM measurement:
Measuring the thickness of K-PHI thin film and the surface morphology was examined using atomic force microscopy (AFM) measurements (SHIMADZU, SPM-9700HT).

Electrical measurement:
Pulse IV measurements were performed using source measurement units (Keysight Technologies, B2912B) and electrical impedance spectroscopy (EIS) was performed using an LCR meter (Keysight Technologies, E4980A). All the measurements were performed using a 4-probe system at room temperature under atmospheric conditions. The pyZwx software was used to obtain the impedance spectrum and fitted under appropriate equivalent circuit assumptions.[1] These electrical measurements were performed on an Au (20 nm)/K-PHI/Au/Si device structure where the top Au electrode had a diameter and thickness of 0.1 mm and 20 nm, respectively.

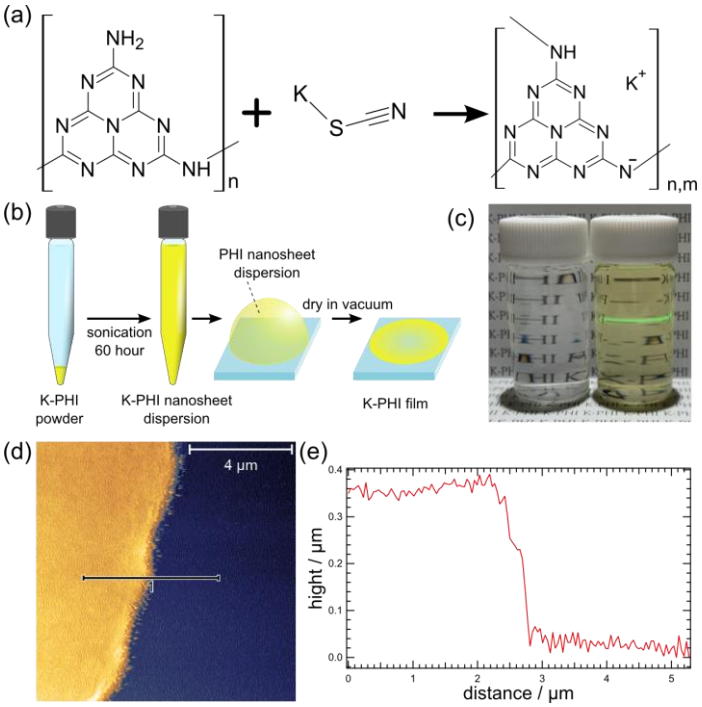

Figure S1. (a) Schematic of K-PHI synthesis. (b) Schematic of K-PHI nanosheet and K-PHI film preparation. (c) K-PHI nanosheet dispersion on the right and NMP solution as a reference on the left. Although the K-PHI nanosheet dispersion is transparent solution, the irradiated laser beam is scattered, indicating that it is a colloidal solution. (d), (e) AFM image of K-PHI film and its line profile in the image. The left side in the image indicates K-PHI film and right side indicates the substrate.

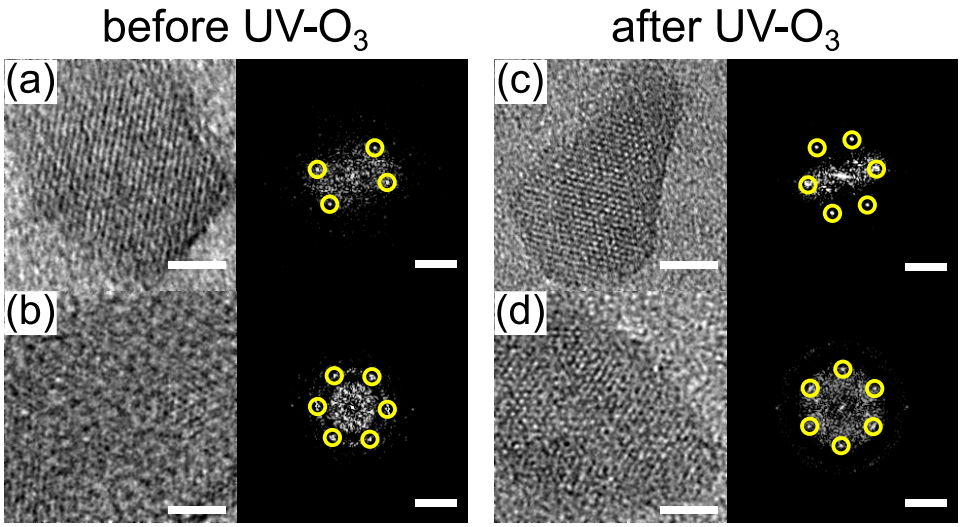

Figure S2: TEM images of K-PHI nanosheet. (a),(b) TEM and FFT images of K-PHI nanosheet before UV-O_3 cleaning. (c),(d) TEM and FFT images of K-PHI nanosheet after UV-O_3 cleaning.

In the sample before UV-O_3 cleaning, a clean lattice image is not observed because of NMP adsorbed on the surface. Therefore, after the cleaning, a fine lattice image can be obtained. The sample after cleaning shows no defects in the structure even after ozone cleaning.

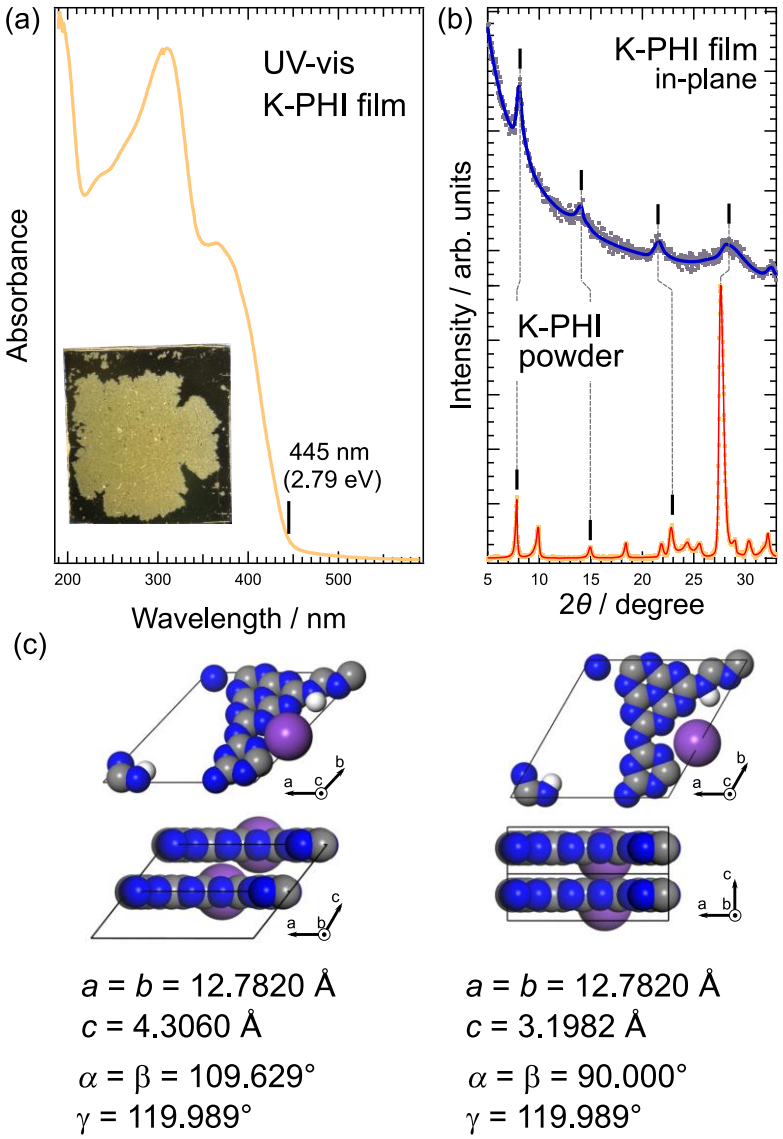

Figure S3. (a) UV-vis spectrum of K-PHI film. The figure shows a photograph of a K-PHI film fabricated on a gold substrate. The black vertical line in the UV-vis spectrum indicates the optical gap of the K-PHI film. (b) XRD patterns of K-PHI film and K-PHI powder. (c) Model of the crystal structure used to simulate the XRD patterns of K-PHI powder and K-PHI film. The blue, black, white, and purple spheres in the structure represent nitrogen, carbon, hydrogen, and potassium ions, respectively.

2. Note 2.

2-1 Binding energy calibration in XPS data

The calibration method for binding energy in XPS was the accidental carbon adsorption reference method described in ISO 18115-1:2013. This method could be used for the XPS measurements in this study because all samples were once exposed to the atmosphere. Since carbon adsorbed on C 1s was identified in all samples, the peak was corrected to 285.0 eV.

2-2 Spectrum fitting in XPS data

The spectra obtained by XPS measurements were fitted using XPSPEAK41. In fitting, the parameters of some peaks were constrained due to physical or chemical requirements. Concretely, the half-widths of the peaks in the same region were fixed for all orbitals, the area ratio was fixed to 2:1 for the K 2p 3/2 and K 2p 1/2 orbitals due to spin-orbital interactions, and the areas of the three peaks in the N 1s orbital were fixed according to the chemical structure.

Background subtraction for spectra can be carried out by either the Shirley or the Tougaard method, both of which were considered in this study. In addition, both methods of subtracting the background, including or excluding the substructure, were considered in this study. Fig. S4(a) shows the background in each case. Fig. S4(b) shows the backgrounds of the Shirley and Tougaard methods, using the N 1s spectrum of K-PHI as a reference. Although both methods can subtract the background without any problem, the difference between the raw data and the fitted data shown in the upper part of the figure indicates that the Tougaard method shows a difference between the raw data and the fitted data near the maximum value of the peaks. Therefore, it can be said that the Shirley method is able to subtract background more closely.

Fig. S4(c) shows an expanded spectrum of the substructure of K-PHI at N 1s, which shows that the spectra of K-PHI with contamination have only one peak in the substructure, whereas the spectra without contamination have two peaks in the substructure. This indicates that the substructure is a varied factor depending on the surface condition of the sample. Therefore, in this study, we reduced the uncertainty of the spectrum by including the substructure as part of the background when subtracting the background.

2-3 Quantitative Analysis for XPS

In this study, the relative sensitivity factor method (Eq. 1) was used as the quantitative analysis method for XPS, in particular, the average matrix relative sensitivity factor (AMRSF) as described in ISO18118:2015 (Eq. 4). In the AMRSF method, the atomic density in the reference sample is important, as described in ISO18118:2015. However, the material used as the reference sample in this study is a vacuum-deposited thin film, which makes it difficult to accurately calculate the thin film density necessary for the atomic density calculation. Therefore, in this study, instead of determining the relative sensitivity factor of each element, the ratio of the relative sensitivity factors among the elements was calculated. That is, the ratio of relative sensitivity factors between heterogeneous elements in a reference sample, for example, the ratio of nitrogen to carbon or nitrogen to oxygen, was used to calculate the ratio of relative sensitivity factors between elements. In this way, the density of the reference sample can be eliminated in the fraction of top and bottom when calculating the ratio of relative sensitivity factors (Eq. 4). This method was adopted because it was the ratios of carbon to nitrogen and nitrogen to oxygen that were important in this study.

In this study, as a reference sample, we used a deposited film of 3,4,9,10-Perylenetetracarboxylic Diimide (PTCDI), a molecule containing nitrogen, carbon, and oxygen, which is the target of analysis. The PTCDI thin film was measured under the same conditions as the K-PHI and melem samples, and the elemental relative sensitivity factor was calculated from the area of each region of the obtained XPS spectrum, and the average matrix relative sensitivity factor was calculated by considering the composition ratio of PTCDI and the matrix correction term of PTCDI.

Fig. S5 shows the effects of background subtraction, various relative sensitivity factors, and various average matrices as described above. As mentioned in Fig. S4, the Shirley method has a smaller value of χ^2than the Tougaard method. In addition, in the Shirley method, χ^2 is the smallest when there is no substructure. The C/N values calculated by the AMRSF method all include the C/N value of K-PHI within the uncertainty range, but the method without substructure and with Shirley background subtraction has the smallest uncertainty. Therefore, in this study, the C/N and O/N values are discussed using the method that does not include substructure and subtracts background using the Shirley method.

Fig. S5(b) shows the C/N values for each relative sensitivity factor. It is obvious that the method using a reference sample (ARSF, AMRSF method) (Eqs. 3 and 4) shows better C/N values than the method without a reference sample (conventional method) (Eq. 2). This indicates that the use of a reference sample and its atomic density are important in the quantitative analysis of XPS, as described in ISO 18118. Fig. S5(c) also shows the C/N values for different average matrices used in the AMRSF method. It can be seen that the C/N values do not change significantly no matter which material is used as the average matrix. In this study, K-PHI was used as the average matrix. To summarize the quantitative analysis method of XPS in this study, the Shirley method was used for the background of each spectrum, and its end point was set at a position not including the substructure. The AMRSF with K-PHI as the average matrix was used for the relative sensitivity factor.

The expression of each relative sensitivity factor is as follows: the subscripts in unk and ref refer to the measured and reference samples; the subscript i in $X_i, I_i, N_i, Q_i, r_i, \lambda_i, F_i, C_i$ refers to the element; each physical quantity represents the elemental concentration, spectral area, atomic density, elastic scattering correction factor, backscattering correction factor, inelastic scattering mean free path, matrix factor, and number of atoms per unit lattice or unit molecule. Q_i and λ_i were calculated using eal13 from the NIST standard database, and r_i is zero in XPS.

Relative sensitivity factor method:

$$X_i^{unk} = \left(\frac{I_i^{unk}}{I_i^{ref}}\right)\frac{X_i^{ref} N_i^{ref} Q_i^{ref}\left(1 + r_i^{ref}\right)\lambda_i^{ref}}{N^{unk} Q_i^{unk}\left(1 + r_i^{unk}\right)\lambda_i^{unk}} = X_i^{ref}\left(\frac{I_i^{unk}}{I_i^{ref}}\right)F_i \tag{1}$$

Conventional method:

$$I_i^{ref} = X_i^{ref} = 1 \text{ in Eq. (1)} \tag{2}$$

Atomic relative sensitivity factor method (ARSF):

$$F_i = 1 \qquad \text{in Eq. (1)} \tag{3}$$

Average matrix relative sensitivity factor method (AMRSF):

$$\frac{X_{\mathrm{C}}^{\mathrm{K-PHI}}}{X_{\mathrm{N}}^{\mathrm{K-PHI}}} = \frac{I_{\mathrm{C}}^{\mathrm{K-PHI}}}{I_{\mathrm{N}}^{\mathrm{K-PHI}}} \times \frac{I_{\mathrm{N}}^{\mathrm{PTCDI}}}{I_{\mathrm{C}}^{\mathrm{PTCDI}}} \times \frac{F_{\mathrm{C}}^{\mathrm{PTCDI}}}{F_{\mathrm{N}}^{\mathrm{PTCDI}}} = \frac{I_{\mathrm{C}}^{\mathrm{K-PHI}}}{I_{\mathrm{N}}^{\mathrm{K-PHI}}} \times \frac{I_{\mathrm{N}}^{\mathrm{PTCDI}}}{I_{\mathrm{C}}^{\mathrm{PTCDI}}} \times \frac{\lambda_{\mathrm{C}}^{\mathrm{PTCDI}} Q_{\mathrm{C}}^{\mathrm{PTCDI}} C_{\mathrm{C}}}{\lambda_{\mathrm{N}}^{\mathrm{PTCDI}} Q_{\mathrm{N}}^{\mathrm{PTCDI}} C_{\mathrm{N}}} \tag{4}$$

$$\left(\because \frac{F_{\mathrm{C}}^{\mathrm{PTCDI}}}{F_{\mathrm{N}}^{\mathrm{PTCDI}}} = \frac{\lambda_{\mathrm{C}}^{\mathrm{PTCDI}} Q_{\mathrm{C}}^{\mathrm{PTCDI}} N^{\mathrm{PTCDI}}}{\lambda_{\mathrm{N}}^{\mathrm{PTCDI}} Q_{\mathrm{N}}^{\mathrm{PTCDI}} N^{\mathrm{PTCDI}}} = \frac{\lambda_{\mathrm{C}}^{\mathrm{PTCDI}} Q_{\mathrm{C}}^{\mathrm{PTCDI}} (\rho^{\mathrm{PTCDI}} N_{\mathrm{A}} C_{\mathrm{C}} / M^{\mathrm{PTCDI}})}{\lambda_{\mathrm{N}}^{\mathrm{PTCDI}} Q_{\mathrm{N}}^{\mathrm{PTCDI}} (\rho^{\mathrm{PTCDI}} N_{\mathrm{A}} C_{\mathrm{N}} / M^{\mathrm{PTCDI}})}\right)$$

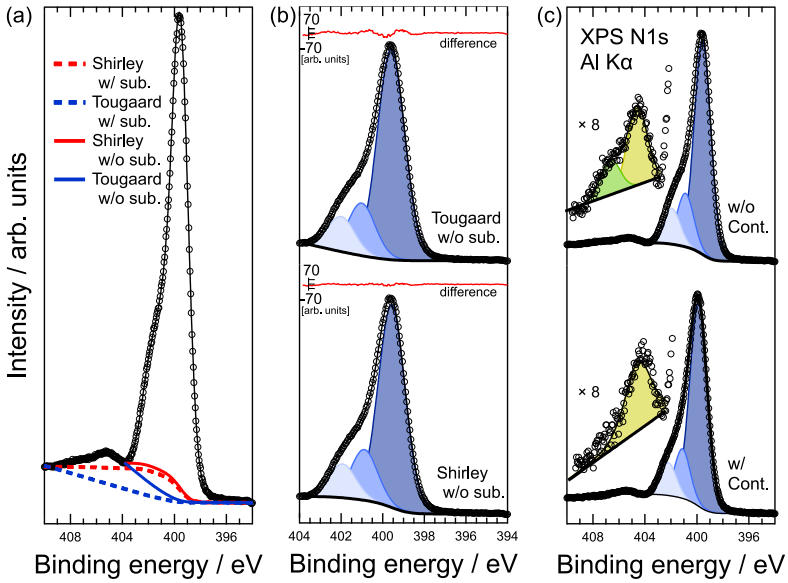

Figure S4.(a) The background treatment used in this study. The red solid and dotted lines indicate the backgrounds obtained by the Shirley method, and the blue solid and dotted lines indicate the backgrounds obtained by the Tougaard method. The solid line indicates the case where the substructure is not included in the end point of the background, and the dotted line indicates the case where it is included. (b) The fitted results and the difference between the raw data and the fitted results are shown for the case where the backgrounds by the Shierly and Tougaard methods are used, using the N 1s spectrum of K-PHI as an example. (c) N 1s spectrum of K-PHI as an example, showing the change of substructure structure due to different surface conditions.

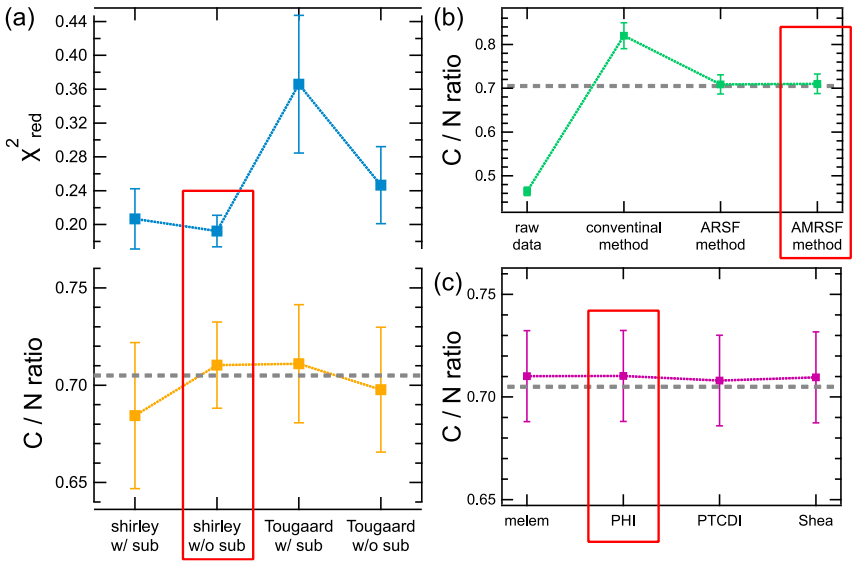

Figure S5. (a)The values of $\chi 2$ and C/N are shown for each of the four background subtraction methods shown in Fig. S4(a). C/N is calculated by the AMRSF method. The gray dotted line in the figure shows the C/N values for K-PHI, and the red box shows the method adopted in this study. (b) C/N values with various relative sensitivity factors; C/N values are calculated by the AMRSF method. The gray dotted line in the figure shows the C/N values for K-PHI, and the red box shows the method adopted in this study. (c) Dependence of the material applied to the average matrix in the AMRSF method is shown. The gray dotted line in the figure shows the C/N values of K-PHI, and the red box shows the method adopted in this study.

2-4 Effect of UV-O_3 cleaning

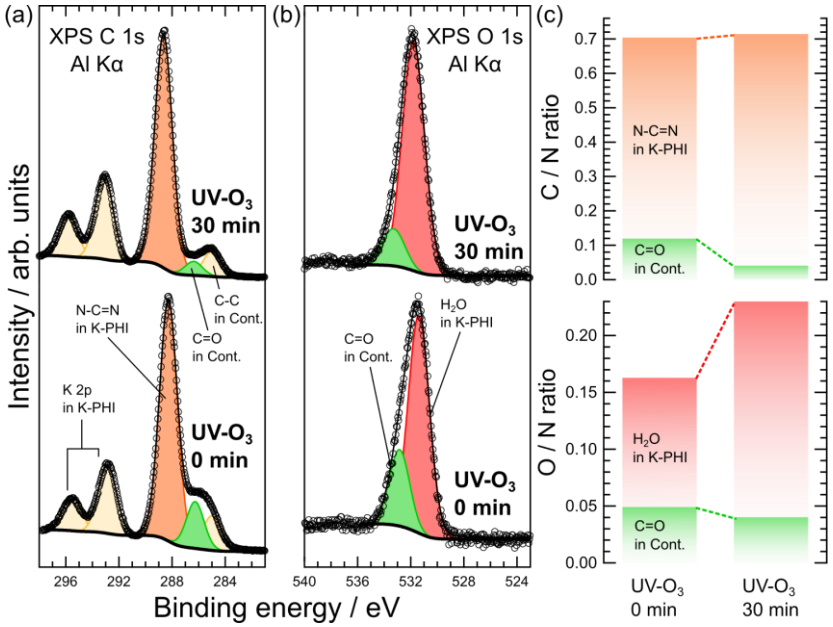

Figure S6. Effects of UV-O_3 cleaning on the K-PHI film. (a), (b) C 1s and O 1s spectra of the K-PHI film before and after O_3 cleaning. The upper and lower panels show the spectra after and before UV-O_3 cleaning, respectively. Attribution of peaks included in K-PHI and contamination is presented near the peaks. Corrections for the background and BE are presented in Note 2 of SI. (c) C/N and O/N values of the K-PHI film before and after UV-O_3 cleaning. The C/N and O/N values are shown in the upper and lower panels, respectively.

Fig. S6(a) and (b) show the C 1s and O 1s spectra of the K-PHI films before and after UV-O_3 cleaning, respectively. UV-O_3 cleaning was performed for 30 min after replacing the cleaning chamber with oxygen. The details of the fitting are described in Note 2 and are the same as the fitting in Fig. 3. The attribution of each peak is shown near the peak. First, the C 1s spectrum revealed that the peak corresponding to C=O decreased with UV-O_3 cleaning. This peak was absent in K-PHI but could be attributed to NMP, which is used as a solvent for preparing K-PHI nanosheets. A C=O peak with BE of ~286 eV was also observed in other materials that can be cleaved using NMP, such as MoS_2 and graphite[2–4]. The green peak in the O 1s spectrum, which was reduced by UV-O_3 cleaning, is attributable to NMP, whereas the red peak is attributable to the K-PHI structure. The peak of water in the K-PHI structure can be reasonably attributed to BE of the adsorbed water molecules on metal and metal oxide surfaces, as the peak appeared at ~532 eV as BE[5–7]. Thus, the C 1s and O 1s results indicate that UV-O_3 cleaning can remove contamination from surface-adsorbed NMP.

Next, we discussed the most critical consideration in UV-O_3 cleaning, i.e., the possible degradation of K-PHI. First, apart from the removal of surface contamination, no spectral change was observed in the C 1s and O 1s spectra before and after UV-O_3 cleaning. The degradation of K-PHI would cause the appearance of new peaks in the C 1s and O 1s spectra. In fact, a new peak appeared at 288–286 eV in the imine-based COF following UV-O_3 cleaning[8]. However, the C 1s and O 1s results of the K-PHI film did not manifest such a change. Fig. S6(c) shows the C/N and O/N values of each peak before and after UV-O_3 cleaning. The C/N values revealed that the K-PHI ratio remained unchanged before and after UV-O_3 cleaning, whereas the ratio of NMP, which is contamination, decreased. Additionally, the O/N values from the contamination decreased. Contrarily, the increase in the O/N values from the water in K-PHI before and after UV-O_3 cleaning was due to the removal of the contaminant layer, thereby easing the access of water molecules to the pores in K-PHI and increasing the number of water molecules in the structure. In summary, the chemical structure of the K-PHI film remained unchanged despite the availability of sufficient O_3 to remove the surface contamination, indicating the high antioxidant capacity of K-PHI.

3. Note 3

3-1 DFT calculation detail

The density of states, partial density of states, and band structures calculated in this study were all obtained using DFT simulations, which were performed in Materials Studio, using Dmol3 as the module, DNP as the Dmol3 basis function, and SCAN, an m-GGA, as the electron correlation approximation method[9–11]. The cutoff radius of the orbitals was set to 10 Å for all calculations, and the number of k-point meshes was set to only Γ points for the `Orbital' calculation, and $9 \times 9 \times 16$, or 1296 points for the other cases.

The cutoff radius was determined from the change in total energy, ionization energy, and electron affinity as the radius is increased from 2 Å to 13 Å. Fig. S7(a) shows the change. It can be seen that both the HOMO and LUMO energies and the total energy are saturated after 8 Å. However, the cutoff radius was set to 10 Å in this study because there was a tendency for the total energy to increase after 10 Å.

3-2 Detail of DFT model

The crystal structure model used for the DFT simulations was basically the one described in Fig. S3. However, the coordination of potassium ions in K-PHI could not be estimated from the results of this study, so it was determined qualitatively using the results obtained from the simulations. Fig. S8 (a) shows the mapping of the electrostatic potential of anionized PHI, i.e., when potassium ion is removed from K-PHI. The electrostatic potentials show that there are three negative potential biases in the PHI anion pore. Therefore, we can say that the potassium ion in K-PHI has three different coordination.

Next, we consider the stacking direction of K-PHI. The simplest model is when potassium ions have the same coordination in all layers, e.g., when all potassium ions are coordinated at position ① in Fig. S8(a) (K-(1,1) model in Fig. S8(b)). However, such a model is not valid. This is because potassium ions in K-PHI approach distances within the vdW radius. Therefore, it is necessary to consider the next simpler model, in which the arrangement of potassium ions differs between the two layers (K-(1,2), (2,3), (3,1) in Fig. S8(b)). In this case, there are a total of three coordination positions for the potassium ion, and unlike the previous case, the system energy is stabilized because the situation where the potassium ion approaches within the vdW radius can be avoided. In fact, the magnitude of the stabilization energy for each model shown in Fig. S8(c) indicates that only the K-(1,1) model is destabilized. In light of these findings, we examine the consistency of the three models of K-PHI with the experimental results in this study.

3-3 Determination of DFT model

The results of the DFT simulations in this study are based on the crystal and chemical structures of K-PHI obtained from Fig. 1 and Fig. 2, but water is not included in the structures. The reasons for this are discussed. The first major reason is that the inclusion of water in K-PHI does not yield appropriate DFT results. This is because water in actual K-PHI is randomly distributed layer by layer, and it is difficult to reproduce such irregularities in the periodic boundary conditions of the model. In fact, several previous studies have reported irregular arrangements of water in crystal structures[12].

The second reason is that the presence or absence of water does not significantly affect the electronic structure of K-PHI. Fig. S9(a) shows the grey, red and blue hatched spectra, which are the actual measured UPS spectra, DOS of the model with water installed in the pores of the K-PHI and DOS of the model without water in the pores of the K-PHI, respectively. Here, the water placed in the pores of the K-PHI does not take into account the randomness of the water. It is clear to see that the difference between the blue and red spectra is small and that the two spectra are almost coincident with the measured UPS spectra. Qualitatively, this means that water molecules in the K-PHI structure have little effect on the electronic structure near the frontier orbitals because they are isolated and do not interact with the K-PHI framework. In fact, the UV-vis spectra of melem, which also has a heptazine framework, do not change depending on the presence or absence of water in the structure, as shown by the results of previous studies[13]. Therefore, the DOS of K-PHI does not change significantly depending on the presence or absence of water in the structure, which does not change the conclusion of this study, and therefore, DFT simulations are performed in the following sections using a model in which water is removed from the K-PHI. Fig. S9(b) shows the DOS and measured UPS spectra of three models of K-PHI with different potassium ion coordination. It can be seen that all spectra contain slight differences but are basically consistent with the shape of the UPS spectra. Therefore, because it is independent from the conclusion of any coordination of the potassium ion, the model of K-(3,1), which is more similar to the UPS spectrum, was adopted in this work.

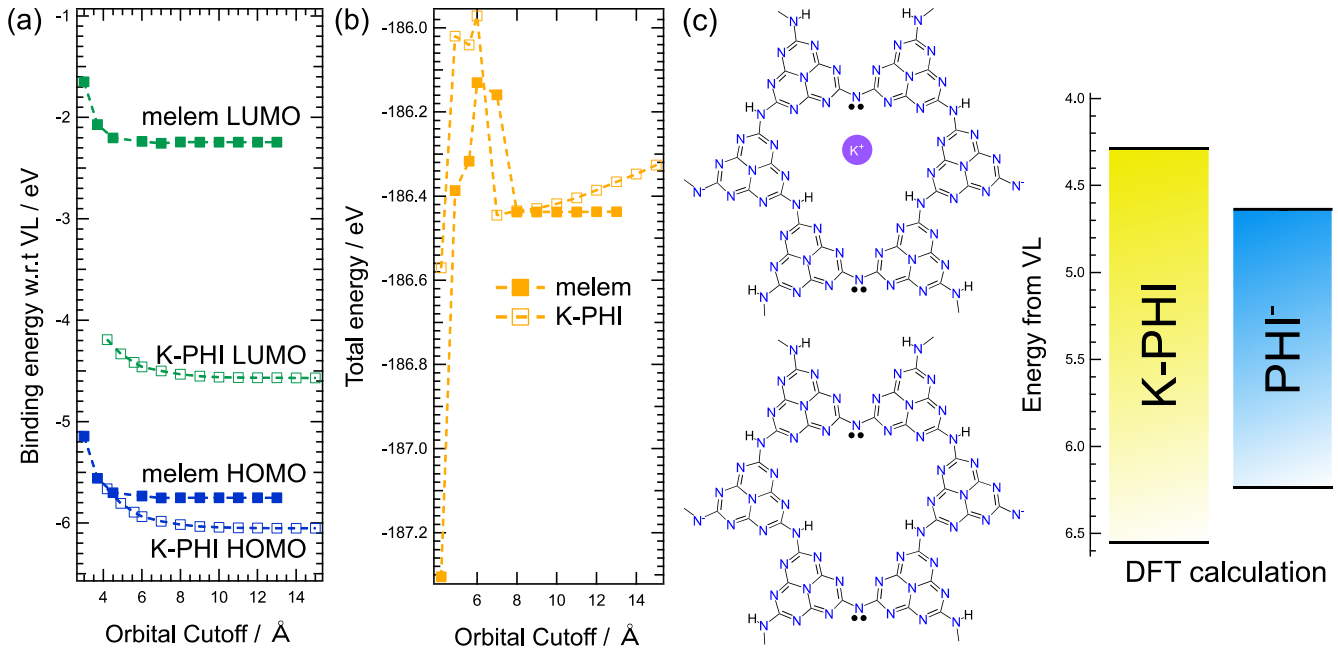

Figure S7. (a) The cutoff radii of the basis functions in the DFT simulations. HOMO and LUMO energies as a function of cutoff radius. The left axis is the binding energy with respect to the vacuum level. (b) Total energy as it varies with cutoff radius. (c) Chemical structure and HOMO/LUMO energies of K-PHI and PHI anion (PHI^-) with potassium ion removed from K-PHI. The left axis is the binding energy with respect to the vacuum level.

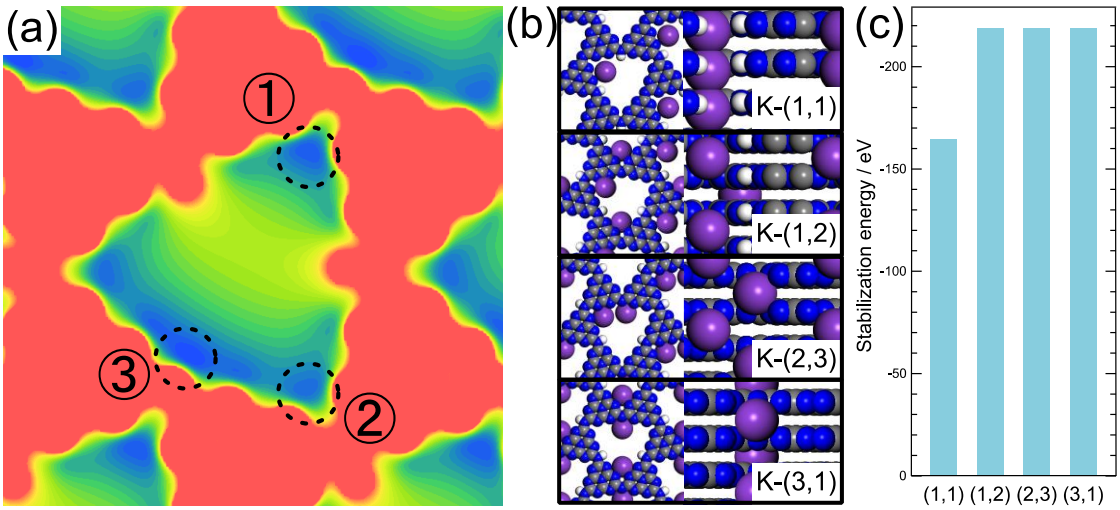

Figure S8. (a) Mapping of electrostatic potentials in PHI anions with potassium ions removed from K-PHI. The numbers in the figure indicate points with low potentials in the PHI anion pore, where potassium ions could be coordinated. (b) Models with different coordination positions for potassium ions in K-PHI; K-(n,n) (n=1, 2, 3) correspond to the numbers in the figure in (a). (c) Stabilization energies for each model.

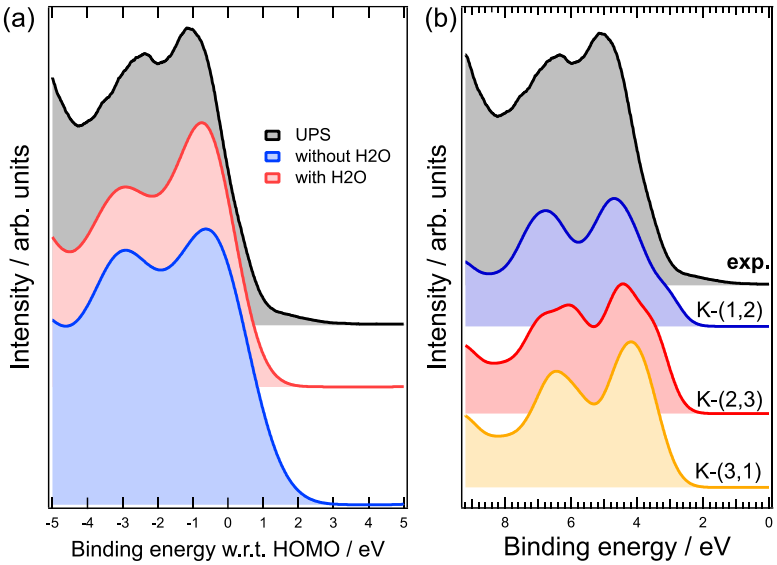

Figure S9.(a) DOS with and without water in the pores in K-PHI; the lower panel shows the results for the K-PHI model without water and the upper panel for the K-PHI model with water. (b) UPS spectra in K-PHI film and density of states obtained from the K-(1,2), (2,3), and (3,1) models shown in Fig. S8(b).

4. Electrical properties

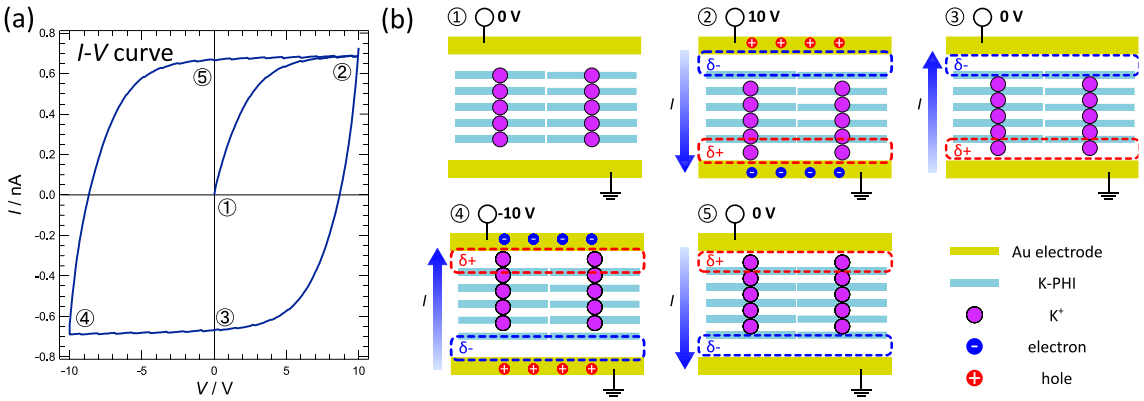

Figure S10. (a) IV characteristics in K-PHI. Electric fields are swept in the order of 1, 2, 3, 4, and 5. (b) Schematic image of the polarization of potassium ions in K-PHI at each voltage value. Yellow and blue rectangles indicate gold and K-PHI. The purple circles indicate potassium ions, and the blue and red circles indicate electrons and holes. The blue arrows indicate the direction of the current.

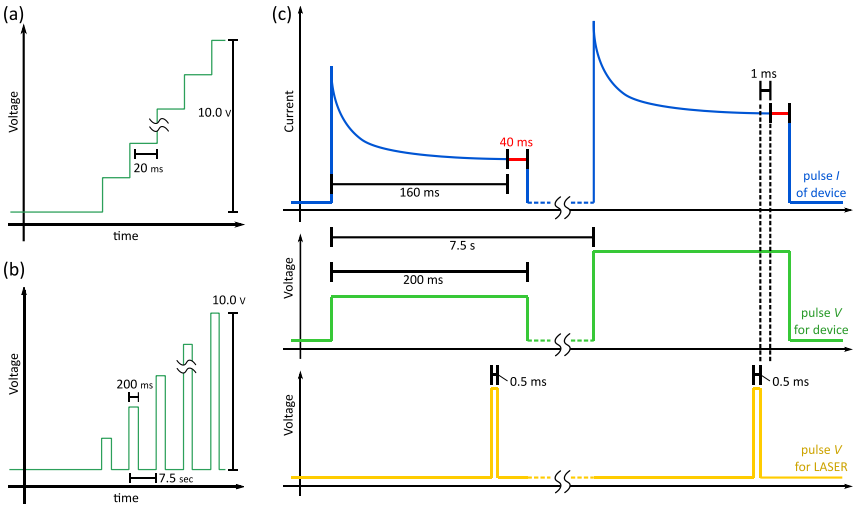

Figure S11 (a), (b) Conceptual diagram of the electric field sweep for IV and pulse IV measurements. For IV measurements, voltage was applied for 20 ms per step; for pulse IV measurements, voltage was applied for 200 ms per pulse, with 7.5 s between pulses. (c) Detail of the voltage pulses in the pulse IV measurement. The timing of the current measurements was 160 ms after the application of the voltage. The timing of the light irradiation was 0.5 ms before the timing of the current measurement.

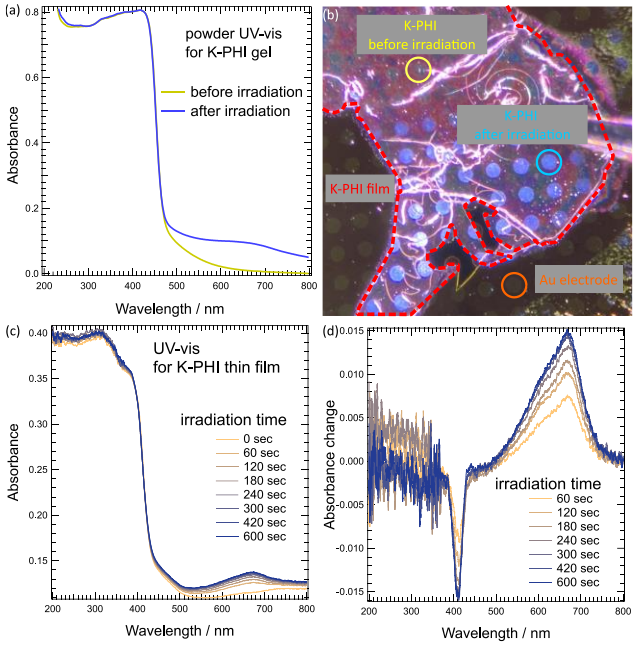

Figure S12. (a) UV-vis spectrum of K-PHI powder. After light irradiation, the absorption around 650 nm is increased. (b) The photo of K-PHI film exposed to light. The orange circle is the gold electrode, and the red dotted line is the K-PHI film. (c) UV-vis spectra of K-PHI thin film. The color of each graph corresponds to the irradiation time, and the light irradiation time was performed from 0 s to 600 s. As in the spectrum of K-PHI powder after light irradiation, the absorption around 650 nm is increased. (d) Absorbance difference spectra for each irradiation time with respect to the 0 s spectrum, showing an increase in absorption near 650 nm and a decrease in absorption near 400 nm.

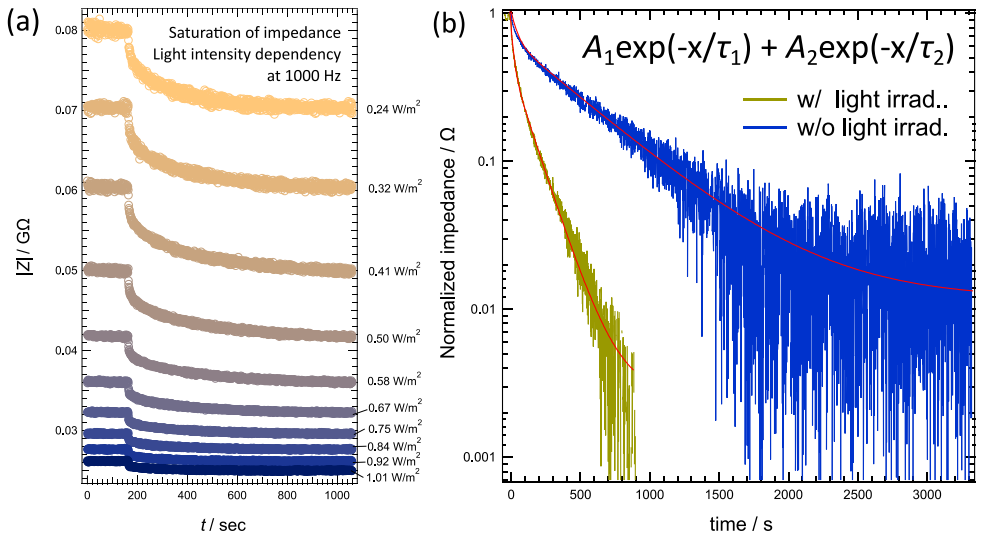

Figure S13 (a) Response of impedance magnitude at each light intensity. For the measurements, the frequency in the measurements was 1000 Hz with light irradiation. The value written on the outside of the right axis is the light intensity of the irradiated light during each measurement. (b) Impedance relaxation process during and after light irradiation in K-PHI. The solid red line in the figure shows the curve of fitting by double exponential.

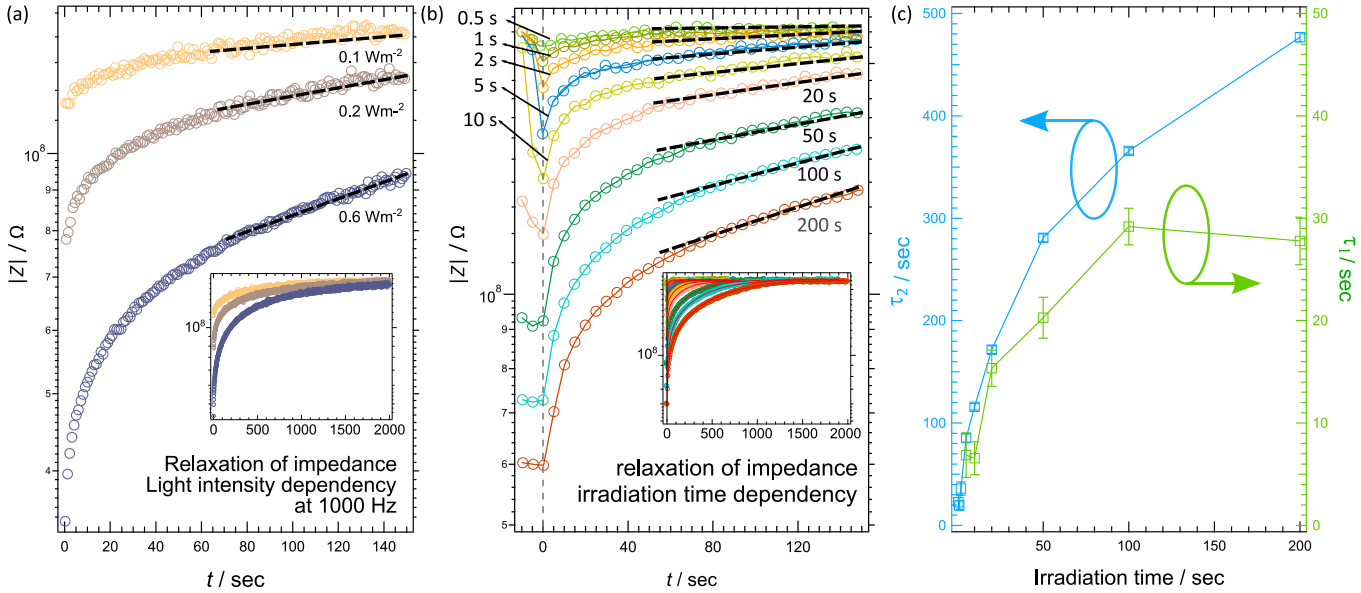

Figure S14 (a) Impedance relaxation process at each light intensity. From top to bottom, light intensity is shown in the order of 0.1 W/m^{-2}, 0.2 W/m^{-2}, and 0.6 W/m^{-2}. The dotted line is an auxiliary line that clearly shows the change in slope. The graph in the figure extends the range of the same data to a longer time period. (b) Impedance relaxation process for each light exposure time. The dotted line is an auxiliary line that clearly shows the change in slope. The graph in the figure extends the range of the same data to a longer time period. (c) The values of τ_1 and τ_2 are plotted for each light exposure time when the data in (b) is fitted with double exp. The left axis shows the value of τ_2 and the right axis shows the value of τ_1.

References

1. Kobayashi K, Suzuki TS. Free analysis and visualization programs for electrochemical impedance spectroscopy coded in python. Electrochemistry. 2021;89(2):218–22.
2. Hernandez Y, Nicolosi V, Lotya M, Blighe FM, Sun Z, De S, et al. High-yield production of graphene by liquid-phase exfoliation of graphite. Nat Nanotechnol. 2008;3(9):563–8.
3. Sim DM, Han HJ, Yim S, Choi MJ, Jeon J, Jung YS. Long-Term Stable 2H-MoS2 Dispersion: Critical Role of Solvent for Simultaneous Phase Restoration and Surface Functionalization of Liquid-Exfoliated MoS2. ACS Omega. 2017;2(8):4678–87.
4. Quirós-Ovies R, Vázquez Sulleiro M, Vera-Hidalgo M, Prieto J, Gómez IJ, Sebastián V, et al. Controlled Covalent Functionalization of 2 H-MoS2 with Molecular or Polymeric Adlayers. Chem - A Eur J. 2020;26(29):6629–34.
5. Yamamoto S, Bluhm H, Andersson K, Ketteler G, Ogasawara H, Salmeron M, et al. In situ x-ray photoelectron spectroscopy studies of water on metals and oxides at ambient conditions. J Phys Condens Matter. 2008;20(18).
6. Yamamoto S, Kendelewicz T, Newberg JT, Ketteler G, Starr DE, Mysak ER, et al. Water adsorption on α-Fe2O3 (0001) at near ambient conditions. J Phys Chem C. 2010;114(5):2256–66.
7. Ali-Löytty H, Louie MW, Singh MR, Li L, Sanchez Casalongue HG, Ogasawara H, et al. Ambient-Pressure XPS Study of a Ni-Fe Electrocatalyst for the Oxygen Evolution Reaction. J Phys Chem C. 2016;120(4):2247–53.
8. Yan D, Wang Z, Cheng P, Chen Y, Zhang Z. Rational Fabrication of Crystalline Smart Materials for Rapid Detection and Efficient Removal of Ozone. Angew Chemie - Int Ed. 2021;60(11):6055–60.
9. Delley B. An all-electron numerical method for solving the local density functional for polyatomic molecules. J Chem Phys. 1990;92(1):508–17.
10. Delley B. From molecules to solids with the DMol3 approach. J Chem Phys. 2000;113(18):7756–64.
11. Sun J, Ruzsinszky A, Perdew J. Strongly Constrained and Appropriately Normed Semilocal Density Functional. Phys Rev Lett. 2015;115(3):1–6.
12. Eaby AC, Myburgh DC, Kosimov A, Kwit M, Esterhuysen C, Janiak AM, et al. Dehydration of a crystal hydrate at subglacial temperatures. Nature. 2023;616(7956):288–92.
13. Dai T, Kiuchi H, Minamide H, Miyake Y, Inoki H, Sonoda Y, et al. Growth and characterization of melem hydrate crystals with a hydrogen-bonded heptazine framework. Phys Chem Chem Phys. 2022;24(22):13922–34.